JOURNAL OF PROPULSION AND POWER
Vol. 23, No. 1, January–February 2007

Modeling and Performance Analysis of the Pulsed Inductive Thruster

Pavlos G. Mikellides* and Chris Neilly†
Arizona State University, Tempe, Arizona 85287-6106

DOI: 10.2514/1.22396

Numerical modeling of the pulsed inductive thruster exercising a time-dependent, two-dimensional, axisymmetric magnetohydrodynamics code provides bilateral validation of the thruster's measured performance and the code's capability of capturing the pertinent physical processes. Computed impulse values for helium and argon propellants demonstrate excellent correlation to the experimental data for a range of energy levels and propellant-mass values. Quantitative energy deposition analysis confirms the thruster's approximately constant-efficiency operation and captures the experimentally observed, critical-mass phenomenon. An idealized model produced a simple impulse expression for this energy range that expands the validity of the aforementioned insights to other propellants and corroborates the thruster's singular operation with ammonia propellant. The simple impulse expression produced compares well with experimental trends and can be used to guide design and optimization of operating conditions.

Nomenclature

B	=	magnetic field
C	=	capacitance
E	=	energy
e	=	specific energy
F	=	thrust
g	=	gravitational acceleration
I	=	impulse
J	=	current
k	=	number of same atoms
L	=	inductance
ℓ	=	number of different atoms
M	=	atomic mass
m	=	propellant mass
n	=	number of electrons
Q	=	ionization energy
R	=	resistance
r, θ, z	=	cylindrical dimensions
r_i	=	inner radius
r_o	=	outer radius
t	=	time
V	=	voltage
Z	=	impedance
δ	=	diffusion depth
η	=	efficiency
μ_o	=	$4\pi \times 10^{-7}$ H/m
ξ	=	energy fraction

Subscripts

c	=	critical
e	=	electron or external
H	=	heavy particle
o	=	stored or initial

Received 11 January 2006; accepted for publication 7 May 2006.

*AST Professor, Department of Mechanical and Aerospace Engineering, P.O. Box 876106; Pavlos.Mikellides@asu.edu. Member AIAA.

†Undergraduate Research Assistant, Honors Program, Department of Mechanical and Aerospace Engineering, P.O. Box 876106. Member AIAA.

I. Introduction

THE pulsed inductive thruster (PIT) is a unique propulsion system due to a combination of its distinctive physical operation, demonstrated performance, and potential advantages over other electric rockets [1]. A spiral induction coil is powered by a series of capacitors in Marx-loop configurations and produces a strong azimuthal electric field once the pulsed current is passed through. The field breaks down the injected propellant over the surface of the flat coil and the associated radial magnetic field induces an azimuthal current within a thin gas layer (Fig. 1). This current interacts with the magnetic field to produce an axially directed electromagnetic force. Such inductive acceleration circumvents the need for electrodes and the erosion-related lifetime limitations that plague traditional electromagnetic thrusters. The PIT could operate with a large range of propellants, however, single-shot operation, as opposed to pulsed operation that would entail multiple shots at a predetermined frequency, demonstrated optimal performance with polyatomic-molecule fuel. Specifically, the PIT-MkV operating with ammonia at 4.6 kJ demonstrated nearly constant efficiencies exceeding 50% for a wide range of specific-impulse values, I_{sp}; $4000 \text{ s} < I_{sp} < 8000 \text{ s}$[1]. Its propensity to work best with such polyatomic fuels renders the thruster as a potentially ideal candidate for water-propellant operation and associated missions such as in situ resource utilization (ISRU) where refueling could be realized by an appropriate water-rich cometary rendezvous or by capitalizing on Lunar, Martian, or Europa's waters for deeper space assignments. Its pulsed operation can provide maneuverability, the aforementioned operation produced an impulse range, I, of $0.05 < I < 0.12$ N-s, which may favor the concept for a number of missions ranging from direct transfers to desired destinations to on-orbit exploration.

To provide added confidence in the PIT's demonstrated capabilities the MACH2 magnetohydrodynamics (MHD) code is employed to model its operation and mutually validate by comparisons to experiments. Specifically, the paper aims to validate the code's capabilities in capturing the pertinent physics by comparing experimental results to the numerical findings and offer valuable insights by computation of energy deposition to various possible energy modes.

II. Numerical Model

MACH2 is a time-dependent, two-dimensional, axisymmetric, multimaterial code that can be applied to problems of complex geometries [2] such as the PIT due to its multiblock structure. The mesh can be refined via a variety of adaptive schemes to capture regions of varying characteristic scale; for the PIT simulations the grid utilized varying grid density by blocks. The set of the

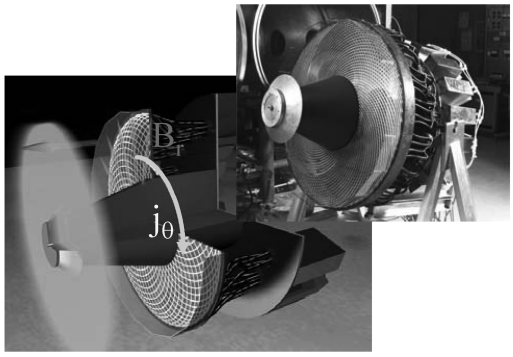

Fig. 1 The pulsed inductive thruster (PIT) and a schematic of the main acceleration process due to the interaction of the applied radial field and the induced azimuthal current.

single-fluid, MHD equations is time advanced with finite-volume spatial differencing, and the boundary conditions are applied via the ghost-cell technique so that no special conditional statement is necessary at the boundaries.

The mass continuity and momentum equations assume a single compressible fluid; however, electrons and ions are in thermal nonequilibrium, and so MACH2 solves two energy equations. Radiation cooling assumed an optically thin plasma at the electron temperature. Evolution of the magnetic field is prescribed by the induction equation that in this case invoked only convection and resistive diffusion. Various models for the plasma resistivity are available. The simulations utilized the classical electron-ion Spitzer–Härm formulation with contributions from electron-neutral collisions applicable to weakly ionized gases [3]. In many engineering applications the source of magnetic flux is applied currents produced from externally applied voltage differentials. For this, the code includes a variety of circuit models such as LRC (inductance-resistance-capacitance), pulse-forming networks, sine waveforms, and several others. The set of the MHD equations is completed by functional relationships for the equations of state that can be either analytic or tabular. The SESAME library [4] is the tabular model that includes semi-empirical models for the thermodynamic properties, opacities, and average ionization state under local thermodynamic equilibrium.

III. Pulsed Inductive Thruster Physical Modeling

A substantial body of experimental data is available for the PIT, comprising a diverse range of propellants, energy levels, and propellant-mass values [1]. The power supply consists of a series of 18 capacitors in Marx-loop pairs that are charged in parallel. This results in an effective discharge voltage that is double that of each capacitor's charge voltage which in turn provides the necessary high electric field for breakdown. In particular, the configuration results in an effective capacitance and voltage that relate to the single capacitance and charge voltage through the total energy available:

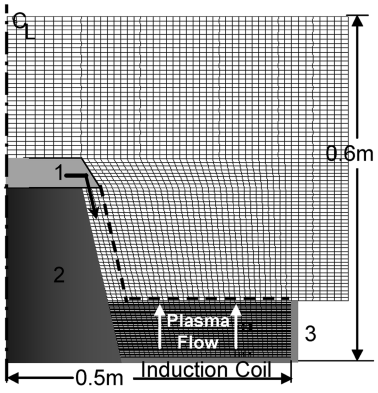

Fig. 2 Schematic of the half-plane thruster with the computational grid utilized (not to scale). 1: Nozzle with pulsed mass valve, 2: conical pylon, 3: confining cuff (lexan).

$$E_o = \tfrac{1}{2}(\text{number of capacitors})CV_o^2 = \tfrac{1}{2}C_{\text{eff}}V_{\text{eff}}^2 \qquad (1)$$

where $V_o = 1/2V_{\text{eff}}$. For the polyatomic propellant experiments the effective capacitance was 9 μF whereas the earlier efforts with monatomic propellants utilized smaller capacitors with effective capacitance of 4.5 μF. The resulting oscillatory current waveform provided a pulse duration of the order of 15 μs with peak currents exceeding 100 kA for a range of charge voltage of $10 < V_o < 16$ kV and propellant mass of $1.5 < m < 10$ mg. Mass is introduced through a nozzle (Fig. 2) by a fast opening gas valve. For optimal distribution of the injected gas the mass pulse is short enough such that it ceases as the leading edge reaches the confining lexan. The thruster's performance experimental data exhibited approximately constant-efficiency trends for a wide range of specific-impulse values ($500 < I_{\text{sp}} < 9000$ s) providing impulses exceeding 0.1 N-s [1]. Monatomic propellants demonstrated efficiencies on the order of 20% while polyatomic propellants with the higher-capacitance bank dramatically improved exhibiting maximum efficiencies above 50% with ammonia.

The MACH2 simulations utilized the helium and argon data for comparisons as the SESAME tables provided a complete real equation of state that includes a degree-of-ionization model. Specifically, the thermodynamic model includes all ionization reactions possible, that is, two for helium and 18 for argon and solves for the thermodynamic properties under the local thermodynamic equilibrium (LTE), that is, assuming a Boltzmann distribution. The physical model included thermal nonequilibrium of a single fluid with classical transport. Boundary conditions modeled thermal and magnetic field insulators with no slip. The computational grid (Fig. 2) extended well downstream of the thruster's exhaust region to comprehensively capture the acceleration process and assure no influence of the outlet boundary conditions that model variables at zero gradient. Grid resolution was maximized in the vicinity of the coil to assure capture of the fast-rising field's diffusion and associated gradient. In particular, the significant acceleration process occurs during the rise time, $t_r \sim 0.9$ μs, which implies a characteristic diffusion depth δ in the range of 1.78–0.533 cm for a 2 –10 eV plasma, (where $\delta = \sqrt{\eta t}$ and $\eta \sim 1000/T_e^{3/2}$ m^2/s is the electrical diffusivity with T_e in eV). The axial grid-cell dimension, $\Delta z = 1.56$ mm (64 cells in the axial direction) assures accurate capture of the field's gradient at a minimum of more than three cells resolving the diffusion depth. Grid sensitivity analysis was performed with double the cell density in the axial direction (128 cells, $\Delta z = 0.78$ mm) to show no effects in the axial distribution of the magnetic field, thus confirming the adequate and least computationally expensive grid density of 64 cells.

Initial conditions assigned uniform density in the vicinity of the coil and along the column extending upstream of the injection nozzle (the confined region identified by the dotted line in Fig. 2), to at best resemble the evolved gas injected from the valve, and uniform room temperature, 300 K. The significance of nonuniformities present due to the injection scheme has been addressed by a separate series of simulations and showed negligible effects when compared to aforementioned simplified initial conditions [5]. These initial conditions assure that ionization of the gas, which occurs after the breakdown, is self-consistently calculated by the MACH2 ionization model along with the evolution of the rest of the pertinent variables, as opposed to an assumed initial ionization state. Emulation of the current waveform used the LRC circuit model. Specifically, a circuit model had been developed [1] to accurately calculate the PIT's current waveform. For the MACH2 simulation the LRC external parameters were adjusted to as best match the important features of the aforementioned model. The comparison is shown in Table 1 and the LRC current waveform used to simulate helium operation is depicted in Fig. 3. It should be emphasized that the PIT circuit model included a semi-empirical statement of the plasma-inductance's axial variation along with the plasma's resistance influence. The MACH2 LRC model is not coupled to the plasma and includes neither contributions. The current calculated from the circuit is implemented

Table 1 Comparison of relevant characteristics of the PIT and LRC emulated waveforms

	PIT	MACH2-LRC
V_{eff}, E:	28 kV, 1764 J	28 kV, 1764 J
$J_{\max}$, t_{rise}:	100 kA, 0.75 μs	100 kA, 0.9 μs
First zero, t_o:	3 μs	2.7 μs
$J_{\min}$:	−40 kA	−22.6 kA

as a magnetic boundary condition at the induction-coil boundary by $B_r(0, t) = \mu_o J(t)/(r_o - r_i)$.

Thrust calculation was performed at the outlet boundaries as the integral of the dynamic pressure and integrated to provide the impulse. This implied that even though the effective pulse duration was about 8 μs, computational times needed to model up to 150 μs so as to capture exhaust of all the propellant through the downstream boundaries. The thrust histogram for the representative case of $V_o = 14$ kV and $m = 3$ mg is shown in Fig. 4 along with the evolution of the impulse. The sharp rise of the thrust value at about 30 μs suggests exhaust of a compact plasma consistent with a slug-acceleration notion. This was confirmed by inspection of the two-dimensional density distribution as calculated by the code; they depicted a fairly sharp mass outline that included the majority of the propellant. The reduced gradient especially after the peak suggests a more dispersed plasma that takes longer to pass through the exhausting boundary. The width of the thrust pulse also indicates the degree of effective coupling and of course the eventual exhaust speed. In other words, a narrower histogram with higher peak thrust values would indicate better coupling and thus increased exhaust velocities for the same propellant mass and energy level. In turn, the aforementioned observations imply a substantially effective coupling of plasma and magnetic flux that allows induction of significant currents and consequently electromagnetic force. Such behavior is quite encouraging as it suggests that MACH2 captures the relevant coupling mechanisms as expected from such a concept.

IV. Validation and Energy Deposition

Computations using the MACH2 code were performed for the range of available charge voltage and propellant mass. Specifically, experiments addressed a range of energy levels between 900 and 1764 J with propellant-mass variation from 0.75 to 9.2 mg. MACH2 was invoked to compute all the different arrangements for a full energy range comparison of impulse vs propellant mass illustrated in Figs. 5–8. The computed impulse correlates very well with the experimental values for all energy and propellant-mass values. This agreement lends confidence in the capability of the code to capture the pertinent acceleration and energy deposition mechanisms and allows for further interrogation of the flow's behavior that can decipher such mechanisms. Insights can be drawn from a quantitative investigation of energy deposition into the different possible modes. For each helium simulation an energy budget was performed to calculate the energy fraction deposited to the internal modes of the propellant (ion/neutral, electron heating and ionization) nonutilized magnetic energy, and radiation dissipation. Specifically, the following energy fraction was formed that represents the dominant energy sinks:

$$\xi = \frac{E_e + E_H + E_{\text{mag}} + E_{\text{rad}}}{E_o} \tag{2}$$

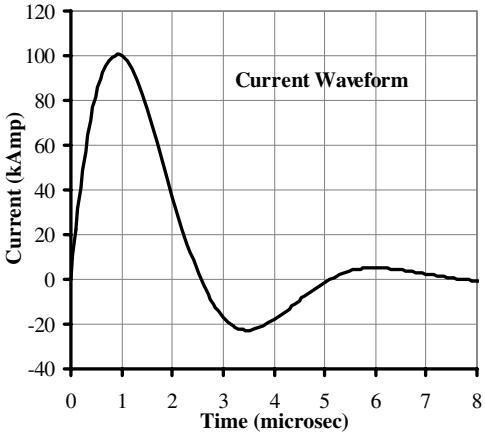

Fig. 3 MACH2 calculated current waveform used to emulate the PIT's circuitry, $V_{\text{eff}} = 28$ kV.

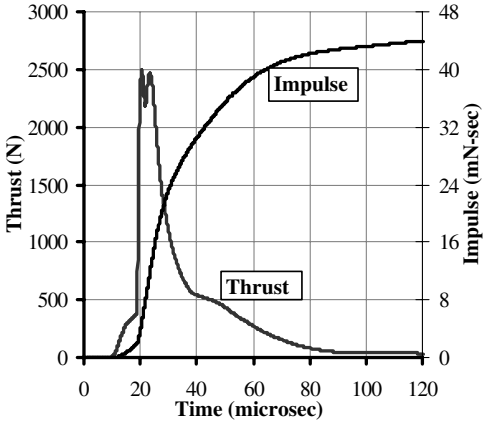

Fig. 4 Calculated thrust histogram and associated impulse for $V_{\text{eff}} = 28$ kV and $m = 3$ mg.

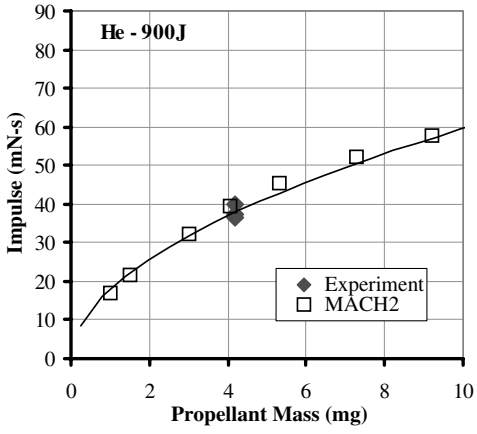

Fig. 5 Comparison of predicted impulse values to experimental data for helium propellant at stored energy of 900 J.

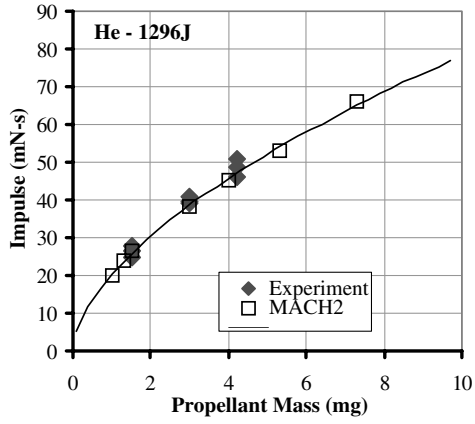

Fig. 6 Comparison of predicted impulse values to experimental data for helium propellant at stored energy of 1296 J.

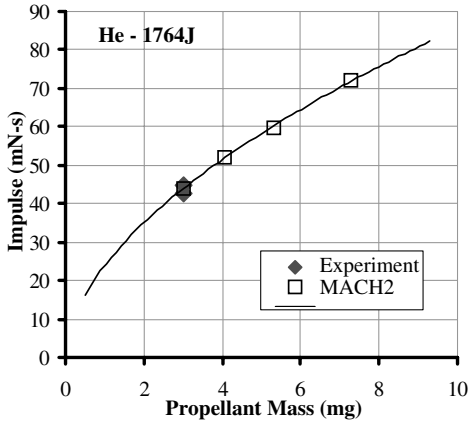

Fig. 7 Comparison of predicted impulse values to experimental data for helium propellant at stored energy of 1764 J.

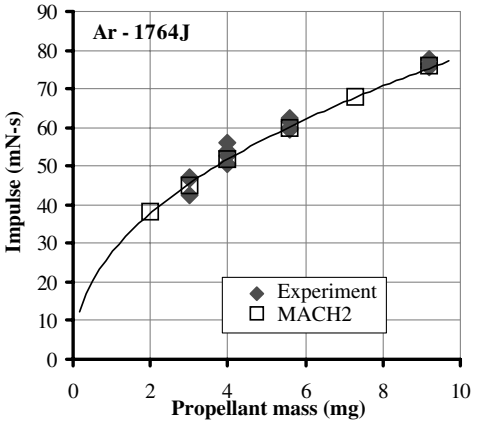

Fig. 8 Comparison of predicted impulse values to experimental data for argon propellant at stored energy of 1764 J.

where E_e and E_H represent energy deposition to the internal energy of the electrons and heavy particles, respectively. The internal energy includes ionization calculated by the SESAME thermodynamic model. The variation of this energy fraction as a function of propellant mass for the three helium energy levels of 900, 1296, and 1764 J is depicted in Figs. 9–11, respectively. The aforementioned energy sinks account for a fraction of about 0.75 of the total energy which in turn is approximately independent of the operating energy level and propellant mass above a certain value. On the other hand, operation below this propellant-mass value depicts a rapid exponential increase of such energy deposition which reflects efficiency degradation since $\eta \sim 1 - \xi$. This rapid deposition to internal energy modes is evocative of the Alfvén critical speed limitation [6] suggested and experimentally supported in steady-state magnetoplasmadynamic (MPD) acceleration. In particular, once the plasma velocity reaches this critical value no significant increase is available until the gas is fully singly ionized. This critical ionization velocity has been linked to the MPD thruster in various ways ranging from the obvious performance limitation to electrode ablation [7] and onset [8]. The latter traditionally refers to experimentally observed voltage fluctuations and data scatter. The same phenomenon seems to be present in operation of the pulsed inductive thruster below a particular "critical-mass" value with both numerical and experimental evidence. Experimentally, operation below this critical-mass value was accompanied by incomplete breakdown and ionization, enhanced data scatter, and a decrease in efficiency [1]. However, the above theoretical predictions suggest that such a phenomenon is accompanied by additional physical processes as MACH2 does not include breakdown models, that is, particle description or some statement regarding the Paschen curve of the particular propellant and assumes axisymmetry. Thus, an equivalent statement to that of the aforementioned Alfvén limitation can be

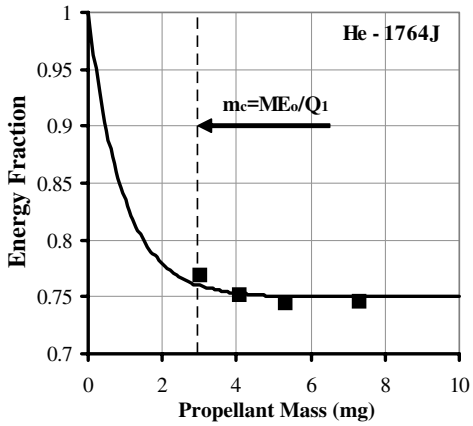

Fig. 9 Calculated energy fraction ξ deposited to energy modes other than kinetic energy for helium propellant $E_o = 1764$ J. The solid line represents Eq. (4).

formulated for PIT operation; *when the operating energy is commensurate to the propellant ionization energy a rapid deposition to internal modes ensues without significant contributions to kinetic energy*. This allows an approximation of the critical mass or better yet normalized with respect to a "critical specific energy,"

$$\text{critical mass: } m_c = \frac{ME_o}{Q_1} \quad \text{or}$$
$$\text{critical specific energy: } e_o^* = \frac{E_o}{m_c} = \frac{Q_1}{M} \tag{3}$$

For helium, $M = 4$ kg/kmol and $Q_1 = 2372.3$ MJ/kmol which approximates the critical mass at the three energy levels as depicted in Figs. 9–11 and identifies the critical specific energy at 593 J/mg (Fig. 12). They adequately capture initiation of ionization energy deposition for all energy levels which supports the suggested mechanism. The statement can be further enhanced and the variation can be more adequately captured by including higher ionization energies and other propellants and incorporating the expected exponential nature of the deposition mechanism, as follows:

$$\xi(e_o) = \xi_o + (1 - \xi_o)\exp\left[\frac{-\sum_{i=1}^{n}(Q_i/M)}{e_o}\right] \tag{4}$$

For helium, $n = 2$ and $Q_2 = 5250.5$ MJ/kmol. The approximation using $\xi_o = 0.75$ is compared to the MACH2-predicted energy fraction in Figs. 9–11 with good agreement, further supporting the nature of ionization energy deposition and usefulness of the expression to guide the experimental design of the operating conditions for any energy and propellant types. The critical specific

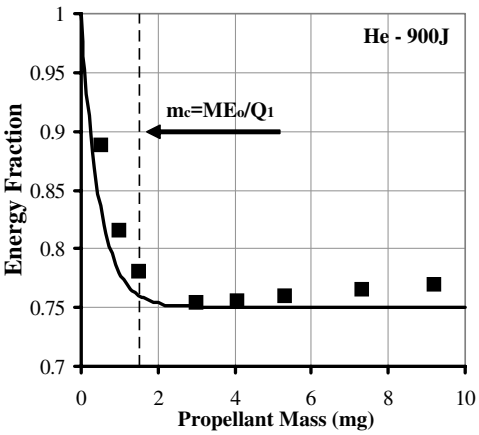

Fig. 10 Calculated energy fraction ξ deposited to energy modes other than kinetic energy for helium propellant $E_o = 900$ J. The solid line represents Eq. (4).

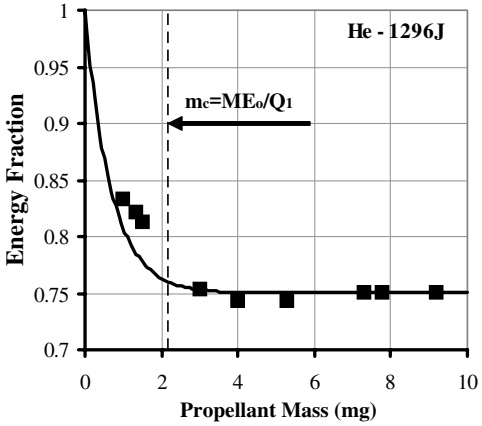

Fig. 11 Calculated energy fraction ξ deposited to energy modes other than kinetic energy for helium propellant $E_o = 1296$ J. The solid line represents Eq. (4).

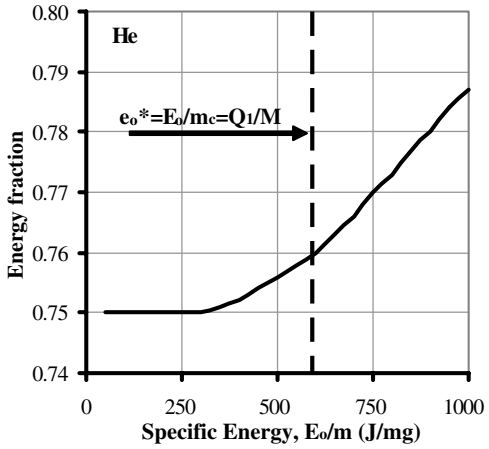

Fig. 12 Calculated energy fraction ξ, Eq. (4), as a function of specific operating energy for helium propellant.

energy value is independent of ξ_o and can be captured by simply evaluating the ratio, $(\xi - \xi_o)/(1 - \xi_o)$. For helium at 593 J/mg the ratio is 0.04 indicating the onset of internal energy deposition. The same criterion can be used to evaluate critical specific energy for more complex atoms or molecules. For example, calculation of the pertinent ratio based on Eq. (4) for argon determines that the critical specific energy is in excess of 10^4 J/mg which implies that operation with argon propellant within this energy range does not exhibit the rapid internal energy deposition.

These insights have led to the development of an idealized model that aims to predict impulse for the PIT extended to other propellants within the energy range addressed above.

V. Idealized Model

To gain further insight into the acceleration mechanism of the PIT, we will construct an idealized model by assuming a purely radial magnetic field that is radially and azimuthally uniform. This can be formulated by the following expression (see Fig. 13), and boundary conditions:

$$B_r(z) = \frac{\mu_o J}{r_o - r_i} f(\zeta) \tag{5}$$

where $\zeta = z/z_o$ and $f(0) = 1$, $f(1) = 0$,

$$\frac{\mathrm{d}}{\mathrm{d}\zeta} f(\zeta)|_{\zeta=1} = f'(1) = 0$$

The function $f(\zeta)$ is arbitrary provided it satisfies the stated boundary conditions subject to an effective current conduction zone z_o.

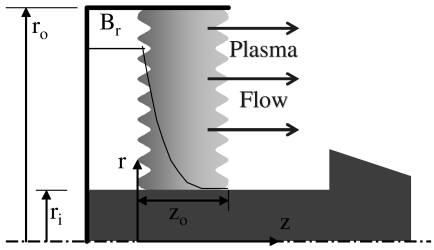

Fig. 13 Schematic of the pulsed inductive thruster utilized for the idealized model.

Application of Ampere's law produces an expression for the induced azimuthal current,

$$\nabla \times \boldsymbol{B} = \frac{1}{z_o}\frac{\partial B_r}{\partial \zeta} = \mu_o j_\theta \Rightarrow j_\theta = \frac{J f'(\zeta)}{(r_o - r_i) z_o} \tag{6}$$

Then the purely axial electromagnetic force exerted on the plasma can be formulated:

$$\begin{aligned} F_z &= \int_V j_\theta B_r \,\mathrm{d}V \int_0^1 \int_0^{2\pi} \int_{r_i}^{r_o} \frac{-\mu_o J^2 f(\zeta) f'(\zeta)}{(r_o - r_i)^2} r \,\mathrm{d}r \,\mathrm{d}\theta \,\mathrm{d}\zeta \\ &= \frac{-\pi \mu_o J^2 \left(r_o^2 - r_i^2\right)^1}{(r_o - r_i)^2} \int_0^1 f(\zeta) f'(\zeta) \,\mathrm{d}\zeta \end{aligned} \tag{7}$$

The value of the integral involving the axial distribution is independent of the function $f(\zeta)$ so long as it adheres to the boundary conditions; it is $-1/2$. Hence, the accelerating force is

$$F_z(t) = \frac{\pi \mu_o J(t)^2 (r_o + r_i)}{2(r_o - r_i)} = \frac{1}{2} \acute{L} J(t)^2 \Rightarrow \acute{L} = \frac{\pi \mu_o (r_o + r_i)}{(r_o - r_i)} \tag{8}$$

where $\acute{L}$ is the inductance per unit length.

If we further assume an LRC circuit configuration for the PIT we can write the governing differential equation as follows:

$$\begin{aligned} V(t) - L_e \dot{J}(t) - R_e J(t) - V_p(t) = 0; \\ V_p(t) = L_p(t) \dot{J}(t) + [R_p(t) + \dot{L}_p(t)] J(t) \end{aligned} \tag{9}$$

where the subscript e denotes the circuit's external elements and subscript p denotes plasma parameters. For the idealized approach we will assume constant effective values for the plasma elements. We can identify the plasma's impedance as $Z = R_p + \dot{L}_p$, and because the plasma's inductance is $L_p = \acute{L} z_0$ we can combine to produce the idealized circuit equation:

$$V(t) - L \dot{J}(t) - [R_e + Z] J(t) = 0 \tag{10}$$

where $L = L_e + \acute{L} z_o$. The solution to the differential equation is the familiar LRC circuit waveform,

$$J(t) = \frac{V_o}{\omega L} \exp\left[\frac{-(R_e + Z)}{2L} t\right] \sin(\omega t); \qquad \omega = \sqrt{\frac{1}{LC} - \frac{(R_e + Z)^2}{4L^2}} \tag{11}$$

that allows calculation of the following convenient integral to be used throughout the remainder of the model's formulation,

$$\begin{aligned} \int_0^\infty J(t)^2 \,\mathrm{d}t &= \int_0^\infty \left(\frac{V_o}{\omega L} \exp\left[\frac{-(R_e + Z)}{2L} t\right] \sin(\omega t)\right) \mathrm{d}t \\ &= \frac{C V_o^2}{2(R_e + Z)} = \frac{E_o}{(R_e + Z)} \end{aligned} \tag{12}$$

Then the total impulse generated by the accelerator is given by

$$I = \int_0^\infty F_z(t)\,\mathrm{d}t = \frac{1}{2}\acute{L}\int_0^\infty J(t)^2\,\mathrm{d}t = \frac{\acute{L}E_o}{2(R_e+Z)} \tag{13}$$

and because $I = mU_e$ we can formulate an expression for the plasma's kinetic energy (KE) and the energy dissipated to the circuit's external elements via resistive loss, E_R

$$\mathrm{KE} = \frac{1}{2}mU_e^2 = \frac{(\acute{L})^2E_o^2}{8m(R_e+Z)^2}; \qquad E_R = R_e\int_0^\infty J(t)^2\,\mathrm{d}t = \frac{R_eE_o}{(R_e+Z)} \tag{14}$$

A simple statement of conservation of energy that distinguishes these two energy modes can be written as $E_R + \mathrm{KE} = (1-\xi)E_o$, where ξ is the fraction of the total energy deposited into the plasma via resistive heating along with magnetic field stored energy. Substitution of the expressions stated above results in a second-order polynomial with respect to the quantity, $R_e + Z$, the positive root of which can be easily expressed as follows:

$$(1-\xi)(R_e+Z)^2 - R_e(R_e+Z) - \frac{\acute{L}^2E_o}{8m} = 0$$

$$\Rightarrow R_e + Z = \frac{R_e + \sqrt{R_e^2 + (1-\xi)\acute{L}^2E_o/2m}}{2(1-\xi)} \tag{15}$$

Substitution into the impulse expression with some algebraic manipulation results in

$$I = \frac{(1-\xi)\acute{L}E_o\sqrt{2m}}{R_e\sqrt{2m} + \sqrt{2mR_e^2 + (1-\xi)\acute{L}^2E_o}}; \qquad \acute{L} = \frac{\pi\mu_o(r_o+r_i)}{(r_o-r_i)} \tag{16}$$

where the expression for the inductance per unit length is repeated for convenience. We note that as the external circuit element losses are diminished ($R_e \to 0$) or as the propellant mass m is decreased, impulse tends toward a maximum that is a function of the square root of the propellant mass and is independent of the plasma's inductance per unit length. The impulse expression allows calculation of the efficiency $\eta = I^2/2mE_o$ along with verification by comparisons to experimental data. The latter is accomplished by using the experimentally deduced external resistance [1], $R_e = 5$ mΩ, along with the PIT's geometry ($r_o = 0.5$ m, $r_i = 0.2$ m) for a range of propellant masses and energy levels operating with different propellants. Before the comparisons it is convenient to express the pertinent performance parameters as a function of the specific operating energy e_o and repeat the energy mass fraction expression, as follows:

$$U_e = \frac{I}{m} = \frac{(1-\xi)\acute{L}e_o}{R_e + \sqrt{R_e^2 + 1/2(1-\xi)\acute{L}^2e_o}}$$

$$\eta = \frac{U_e^2}{2e_o}$$

where

$$\xi = \xi_o + (1-\xi_o)\exp\left[\frac{-\sum_{i=1}^n (Q_i/M)}{e_o}\right]$$

for atoms,

$$\xi = \xi_o + (1-\xi_o)\exp\left[\frac{-\sum_{j=1}^{\ell} k\sum_{i=1}^n (Q_i/M_j)}{e_o}\right] \tag{17}$$

for molecules. Dissociation energy has been neglected as in general it will not substantially affect prediction of the critical mass, but it can be easily incorporated. (For NH_3 the dissociation energy is 152 J/mg which is less than 10% of the critical energy at 1800 J/mg.) Such comparisons are displayed in Figs. 14–19 for helium, argon, carbon dioxide, and ammonia propellants which show effective exhaust velocity and efficiency as a function of specific operating energy e_o.

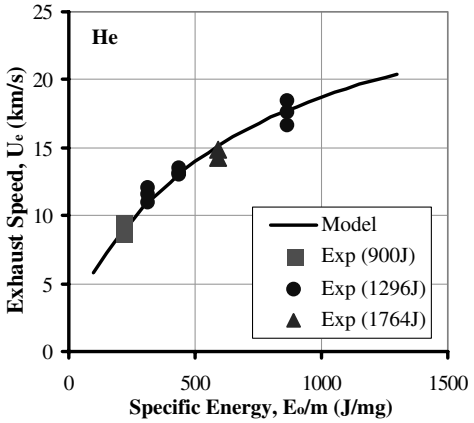

Fig. 14 Exhaust speed comparison of the idealized model Eq. (17) to experimental data for helium propellant $\xi_o = 0.77$.

The comparisons for this energy range highlight a few unexpected trends. For all four propellants addressed, the experimentally deduced effective exhaust velocity values I/m are adequately captured by the model, Eq. (17), by using a constant value for ξ_o. This implies that the fraction of the total available energy expended in resistive heating and stored in the magnetic field before ionization onset is independent of the propellant mass and energy level. Furthermore, for He, Ar, and CO_2 this value is independent of

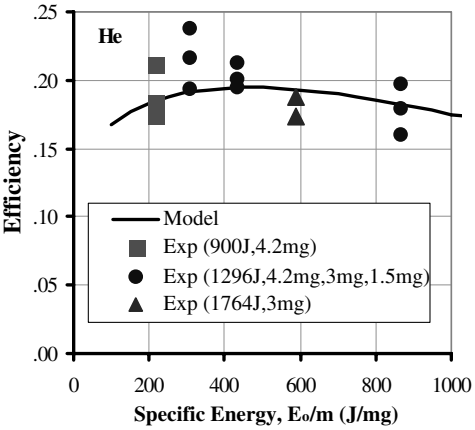

Fig. 15 Efficiency comparison of the idealized model Eq. (17) to experimental data for helium propellant $\xi_o = 0.77$.

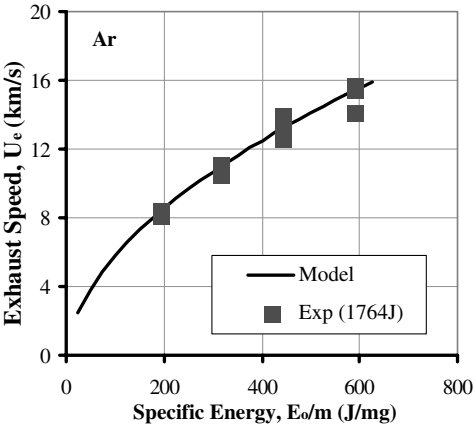

Fig. 16 Exhaust speed comparison of the idealized model Eq. (17) to experimental data for argon propellant $\xi_o = 0.77$.

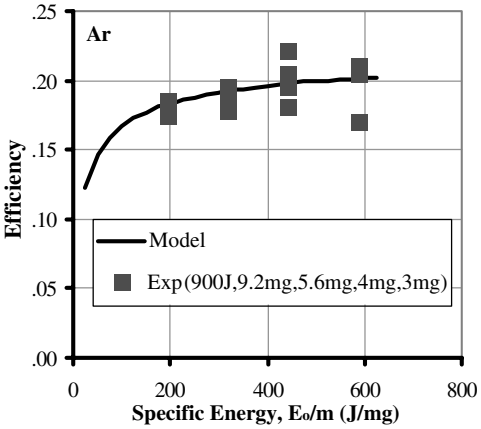

Fig. 17 Efficiency comparison of the idealized model Eq. (17) to experimental data for argon propellant $\xi_o = 0.77$.

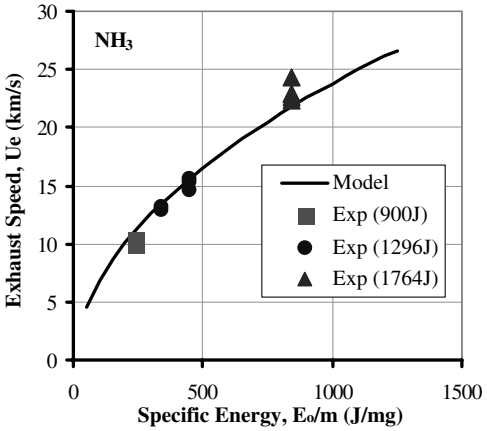

Fig. 19 Exhaust speed comparison of the idealized model Eq. (17) to experimental data for ammonia propellant $\xi_o = 0.69$.

propellant type as well; it is constant at $\xi_o = 0.77$, but NH_3 is an exception as exhaust speed is captured with $\xi_o = 0.69$. (The value of the constant ξ_o for helium was augmented from the previous 0.75 value to account for small radial momentum losses that were not included in the calculation of ξ predicted by MACH2.) In other words, the idealized model indicates that for all these propellants the efficiency cannot exceed 23% regardless of propellant-mass value and energy level, with the ammonia exception that exhibits a maximum of 31%. (The PIT operating with NH_3 propellant exhibited 50% efficiency only at higher energy levels.) This is demonstrated by the efficiency vs specific operating energy along with further trends. The variation of the thruster's efficiency operating with He propellant, Fig. 15, exhibits a maximum value along with the decrease in efficiency beyond the critical specific energy value, $\sim$593 J/mg. The efficiency decreases below the maximum value as a consequence of the increasing significance of the external resistance R_e term, consistent with the efficiency expression approaching zero as operating specific energy tends toward zero. The nature of the argon efficiency variation, Fig. 17, is substantially different than that of helium as it does not exhibit a similar efficiency degradation. The efficiency monotically increases toward the maximum value, which is consistent with the fact that the critical specific energy value is well above the maximum specific operating energy for this set of experiments. The agreement between model and experiment confirms the insight. The case is the same for CO_2 and NH_3 which would exhibit the same monotonic increase as both operated below critical specific energy. [For NH_3 the critical specific energy is above 1800 J/mg according to the ξ expression from Eq. (17).]

The aforementioned trends suggest similar mechanisms for energy deposition regardless of propellant type, energy level, and mass value which is quite remarkable along with further confirmation of the PIT's demonstrated approximately constant efficiency for a range of specific-impulse values [1]. Ammonia propellant is an exception, even though the constant value for ξ_0 still implies constant efficiency for a range of propellant-mass values, as the model identifies a decreased amount of energy deposition to modes other than kinetic energy and thus justifies the demonstrated increased efficiency with this propellant. The explanation can only be deciphered by proper numerical modeling with ammonia propellant that includes an appropriate model for its thermodynamic properties including degree of ionization.

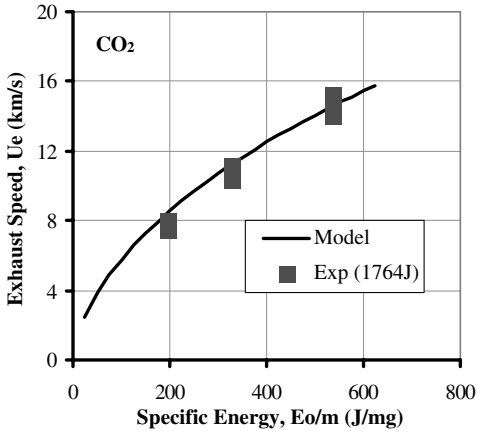

Fig. 18 Exhaust speed comparison of the idealized model Eq. (17) to experimental data for carbon dioxide propellant $\xi_o = 0.77$.

VI. Conclusions

The magnetohydrodynamic code MACH2 was utilized to model the pulsed inductive thruster's operation and offer insights to its demonstrated performance. Time-dependent, two-dimensional axisymmetric simulations were performed for operation with helium and argon propellants for energy levels below 1764 J and a wide range of propellant-mass values. Comparison of computed impulse to experimental data is excellent lending confidence in the code's ability to capture the pertinent physical mechanisms and allowing further interrogation into the nature of energy deposition to different modes. Such quantitative analysis showed that energy deposition to modes other than kinetic energy is independent of the propellant-mass value above a critical-mass value. This confirms the approximately constant-efficiency operation demonstrated by the PIT for a wide range of specific-impulse values. In addition, the code also captured the increased deposition to energy sinks below the critical-mass value also observed by experiment through a decrease in efficiency. An idealized model produced a simple expression for impulse that confirmed and extended the insights to propellants other than the ones addressed by the simulations and also confirmed the unique nature of ammonia by identifying the decreased energy fraction deposited to undesired energy modes. Specifically, the model captured experimental trends for all propellants, quantified the critical-mass phenomenon, confirmed the approximately constant-efficiency operation for a range of specific operation energy, and can be easily used to guide experimental design and performance optimization.

Acknowledgments

The authors would like to especially acknowledge Ralph Lovberg for provision of the experimental data used for validation along with invaluable input to our effort. The authors also acknowledge Northrup-Grumman Corporation for use of the PIT image appearing in Fig. 1.

References

[1] Dailey, L. C., and Lovberg, R. H., "The PIT MkV Pulsed Inductive

Thruster," NASA CR 191155, July 1993.
[2] Frese, M. H., "MACH2: A Two-Dimensional Magnetohydrodynamics Simulation Code for Complex Experimental Configurations," Mission Research Corporation, AMRC-R-874, Los Alamos, NM, Sept. 1986.
[3] Degnan, J. H., and Peterkin, R. E., Jr., "Compact Toroid Formation, Compression, and Acceleration," *Physics of Fluids*, Vol. B5, No. 8, 1993, pp. 2938–2945.
[4] Holian, K. S., "T-4 Handbook of Material Properties Data Base. Vol Ic: EOS," Los Alamos National Laboratory LA-1160-MS, Los Alamos, NM, Nov. 1984.
[5] Mikellides, P. G., "Numerical Simulations of the Pulsed Inductive Thruster," *Space Technology and Applications International Forum Proceedings*, ISBN 0-7354-0115-2, Vol. 654, 2003, pp. 540–546.
[6] Alfvén, H., "Collision Between a Nonionized Gas and Magnetized Plasma," *Reviews of Modern Physics*, Vol. 32, No. 4, 1960, pp. 710–713.
[7] Turchi, P. J., "Critical Speed and Voltage-Current Characteristics in Self-Field Plasma Thrusters," *Journal of Propulsion and Power*, Vol. 2, No. 5, 1988, pp. 398–401.
[8] Preble, J. C., "Onset in Magnetoplasmadynamic Thrusters: A Model of Electrothermal Instability," M.S. Thesis, Department of Aeronautics and Astronautics, MIT, May 1990.

R. Myers
Associate Editor